

Near-resonant instability of geostrophic modes: beyond Greenspan's theorem

T. Le Reun ^{1,2,†}, B. Gallet ³, B. Favier ¹ and M. Le Bars ¹

¹Aix Marseille Univ, CNRS, Centrale Marseille, IRPHE UMR 7342, Marseille, France

²DAMTP, University of Cambridge, Wilberforce Road, Cambridge CB3 0WA, UK

³Service de Physique de l'État Condensé, CEA Saclay, CNRS, Université Paris-Saclay

(Received xx; revised xx; accepted xx)

We explore the near-resonant interaction of inertial waves with geostrophic modes in rotating fluids via numerical and theoretical analysis. When a single inertial wave is imposed, we find that some geostrophic modes are unstable above a threshold value of the Rossby number kRo based on the wavenumber and wave amplitude. We show this instability to be caused by triadic interaction involving two inertial waves and a geostrophic mode such that the sum of their eigen frequencies is non-zero. We derive theoretical scalings for the growth rate of this near-resonant instability. The growth rate scaled by the global rotation rate is proportional to $(kRo)^2$ at low kRo and transitions to a kRo scaling for larger kRo . These scalings are in excellent agreement with direct numerical simulations. This instability could explain recent experimental observations of geostrophic instability driven by waves.

1. Introduction

Rotating turbulent flows are ubiquitous in geo- and astrophysical systems such as stellar interiors, planetary cores, oceans and atmospheres. In a large number of numerical simulations and experiments (see the review by Godeferd & Moisy (2015)), rotating turbulence is observed to develop a strong anisotropy and to spontaneously form vortices that are invariant along the rotation axis. The latter correspond to a first-order balance between the Coriolis force and pressure gradients and are called “geostrophic modes”. Yet, the systematic observation of strong geostrophic modes is at odds with various evidence suggesting that rotating turbulence could as well be dominated by inertial waves that are sustained by the restoring action of the Coriolis force. Recent numerical (Le Reun *et al.* 2017) and experimental (Le Reun *et al.* 2019; Brunet *et al.* 2020) studies have shown that injecting energy in waves solely creates a turbulent state comprising of inertial waves only when the forcing amplitude is sufficiently small, *i.e.* a discrete version of inertial wave turbulence (Galtier 2003). It is only at larger forcing amplitudes that a secondary instability leads to the classical geostrophic-dominated turbulence. Asymptotic theories describing rotating turbulence in the limit of vanishing forcing amplitude and dissipation also suggest that waves could dominate over geostrophic modes in such a regime (Bellet *et al.* 2006; Sagaut & Cambon 2018). Hence, although bi-dimensionalisation in the form of geostrophic eddies has been commonly observed, it may not be the only equilibrium state of rotating turbulence, be it at moderate (Yokoyama & Takaoka 2017; Favier *et al.* 2019) as well as small (van Kan & Alexakis 2019) forcing amplitudes. In addition, the nature of the forcing seems fundamental in determining the equilibrium state of rotating turbulence.

† Email address for correspondence: tl402@cam.ac.uk

These results altogether call for a better understanding of the fundamental processes by which waves give rise to balanced geostrophic modes. The studies of Le Reun *et al.* (2019) and Brunet *et al.* (2020) suggest that such a transfer occurs through an instability. Although wave-to-wave interactions are primarily governed by triadic resonance (Bordes *et al.* 2012; Vanneste 2005), they cannot account for wave-to-geostrophic transfers (Greenspan 1969), at least in the asymptotic limit of vanishing velocity amplitude and dissipation. Several alternative mechanisms, outside the framework of Greenspan's theorem, have been proposed. Four-modes interactions can transfer energy from waves to geostrophic flows, either directly (Newell 1969; Smith & Waleffe 1999) or through an instability mechanism (Kerswell 1999; Brunet *et al.* 2020). The growth rate of such an instability scales like Ro^2 , with Ro the dimensionless wave amplitude or Rossby number. It develops over longer timescales than triad-type interactions between waves. The other inviscid mechanism that has been proposed to account for wave-geostrophic transfer is quasi-resonant triadic interaction (Newell 1969; Smith & Waleffe 1999), that is, a triad between waves whose frequencies do not exactly satisfy the resonance condition (Bretherton 1964). Their presence and their role in the bi-dimensionalisation of rotating turbulence has been assessed by several numerical studies (Smith & Lee 2005; Alexakis 2015; Clark di Leoni & Mininni 2016). While it has been shown that such triads can transfer directly energy from two pre-existing waves to geostrophic modes, we show that this transfer can arise spontaneously through an instability mechanism. More precisely, we show with direct numerical simulations (DNS) and theoretical analysis that there exists a linear mechanism by which a single inertial wave drives exponential growth of geostrophic modes through near-resonant triadic interaction.

2. The stability of a single inertial wave

2.1. Governing equations and numerical methods

Let us consider an incompressible fluid rotating at rate $\Omega \mathbf{e}_z$. We investigate the stability of a single plane inertial wave with wave vector \mathbf{k} and eigen frequency ω_k . Its amplitude is proportional to \mathbf{U}_w with

$$\mathbf{U}_w = \mathbf{h}_k^{s_k} \exp i(\mathbf{k} \cdot \mathbf{x} - \omega_k t) + c.c. \quad (2.1)$$

$\mathbf{h}_k^{s_k}$ is a helical mode, that is, when \mathbf{k} is not parallel to the axis of rotation \mathbf{e}_z (Cambon & Jacquin 1989; Waleffe 1992)

$$\mathbf{h}_k^{s_k} = \frac{1}{\sqrt{2}} \left(\frac{(\mathbf{k} \times \mathbf{e}_z) \times \mathbf{k}}{|(\mathbf{k} \times \mathbf{e}_z) \times \mathbf{k}|} + i s_k \frac{\mathbf{k} \times \mathbf{e}_z}{|\mathbf{k} \times \mathbf{e}_z|} \right), \quad (2.2)$$

where $s_k = \pm 1$ is the sign of the helicity of the plane wave. If \mathbf{k} is parallel to \mathbf{e}_z , $\mathbf{h}_k^{s_k} = \mathbf{e}_x + i s_k \mathbf{e}_y$. \mathbf{U}_w automatically satisfies the incompressibility condition since $\nabla \cdot \mathbf{U}_w \propto \mathbf{k} \cdot \mathbf{h}_k^{s_k} = 0$. \mathbf{U}_w satisfies the linearised rotating Euler equation,

$$\partial_t \mathbf{U}_w + 2\Omega \times \mathbf{U}_w = -\nabla \pi_w, \quad (2.3)$$

provided that $\omega_k^{s_k}$ and \mathbf{k} are related by the dispersion relation of inertial waves

$$\omega_k = 2s_k \Omega \frac{k_z}{k} = 2s_k \Omega \cos \theta, \quad (2.4)$$

θ being the angle between the wavevector \mathbf{k} and the rotation axis \mathbf{e}_z (ranging from 0 to π), and $k = |\mathbf{k}|$. We solve for the time evolution of perturbations \mathbf{u} to the wave \mathbf{U}_w

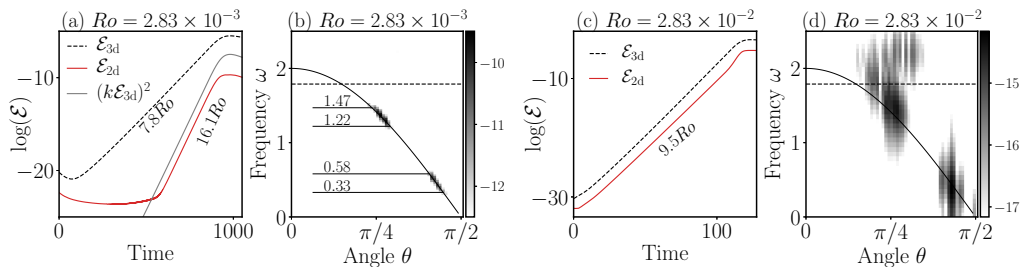


FIGURE 1. Kinetic energy time series (a and c) and heat map of $\log(\mathcal{E}(\theta, \omega))$ (b and d) resulting from two numerical simulations of the stability of the inertial wave $\mathbf{k} = 2\pi [4, 0, 8]$ at $Ro = 2.83 \times 10^{-3}$ and $Ro = 2.83 \times 10^{-2}$. In panels (a) and (c), the labels indicate the slope of the best fit for the exponential growth. In panel (b) and (d), the plain line materialises the dispersion relation of inertial waves and the horizontal dashed line the frequency of the imposed wave ($\omega_k \simeq 1.78$). For the spectral energy maps, the temporal Fourier transforms have been performed until $t = 800$ for panel (b) and $t = 100$ for panel (d). In panel (b), we have indicated the extremal frequencies of the two energy locations.

maintained at a constant amplitude via the following set of equations

$$\partial_t \mathbf{u} + Ro(\mathbf{U}_w \cdot \nabla \mathbf{u} + \mathbf{u} \cdot \nabla \mathbf{U}_w) + \mathbf{u} \cdot \nabla \mathbf{u} + 2\mathbf{e}_z \times \mathbf{u} = -\nabla \pi + E \nabla^2 \mathbf{u} \quad (2.5a)$$

$$\nabla \cdot \mathbf{u} = 0 \quad (2.5b)$$

where time is scaled by Ω^{-1} and length by the domain size L . We have introduced the Ekman number $E = \nu/(L^2 \Omega)$, ν being the kinematic viscosity, and an input Rossby number Ro quantifying the dimensionless amplitude of the plane wave.

Equations (2.5) are solved numerically in a triply periodic cubic box using the code Snoopy (Lesur & Longaretti 2005). The dynamics of the perturbation flow $\{\mathbf{u}, \pi\}$ is determined with pseudo-spectral methods, that is, $\{\mathbf{u}, \pi\}$ is decomposed into a truncated sum of Fourier modes $\{\hat{\mathbf{u}}_{\mathbf{q}}, \hat{\pi}_{\mathbf{q}}\} e^{i\mathbf{q} \cdot \mathbf{x}}$. A wave-vector \mathbf{q} writes $2\pi/L(n_x, n_y, n_z)$ where $n_{x,y}$ are integers varying from $-N$ to N and n_z is an integer ranging from 0 to N because of Hermitian symmetry. In the following, $N = 96$; higher resolutions have been tested and yield the exact same results. The temporal dynamics of the modes $\hat{\mathbf{u}}_{\mathbf{q}}$ is solved using a third order Runge-Kutta method. Note that the size of the box L is artificial and we thus expect our results to depend on the intrinsic Rossby number based on the imposed wavelength kRo rather than Ro alone.

2.2. Numerical results

Keeping the Ekman number to $E = 10^{-6}$, two simulations of the stability of the inertial wave $\mathbf{k} = 2\pi [4, 0, 8]$ (with $s_k = 1$) are performed at low ($Ro = 2.83 \times 10^{-3}$) and moderate ($Ro = 2.83 \times 10^{-2}$) wave amplitudes. They are both initiated with a random noise comprising wavenumbers ranging between 0 and 15π , with very small initial amplitude. The use of spectral methods allows separating the kinetic energy of the perturbation flow \mathbf{u} into a two-dimensional component \mathcal{E}_{2d} , accounting for all modes \mathbf{q} with $q_z = 0$, and a complementary three-dimensional component \mathcal{E}_{3d} . In addition, performing Fourier transform in space and time allows projecting the kinetic energy of \mathbf{u} in the sub-space of the dispersion relation of inertial waves to draw spatio-temporal spectrum $\mathcal{E}(\theta, \omega)$ (Yarom & Sharon 2014; Le Reun *et al.* 2017). Note that, in these maps, θ is restricted to $[0, \pi/2]$ since the flow is real and only the wavevectors \mathbf{q} with $q_z \geq 0$ are simulated due to the Hermitian symmetry. Moreover, the spectra are symmetrised with respect to $\omega = 0$ and the maps are shown as a function of $|\omega|$ to be more compact.

The kinetic energy time series and maps are shown for both simulations in figure 1. At

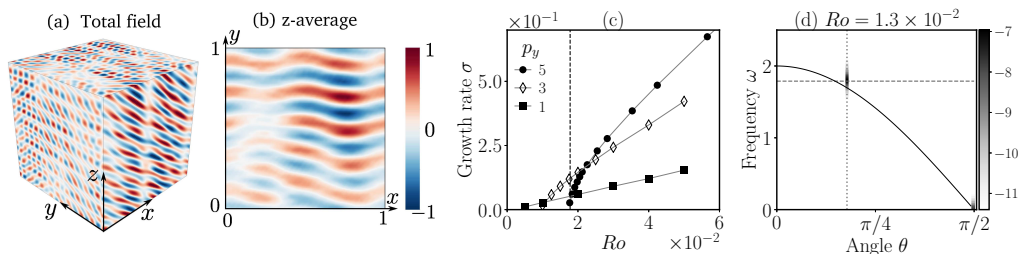


FIGURE 2. (a) Three-dimensional vertical vorticity field of the growing perturbation at $Ro = 2.83 \times 10^{-2}$ and (b) its vertical average. The fields are normalised by their maximum values. (c) Growth rate of the geostrophic modes $\mathbf{p}_g = 2\pi[0, p_y, 0]$ with $p_y \in \{1, 3, 5\}$ as a function of the imposed wave amplitude Ro . The vertical line materialises $kRo = 1$. The lines joining the markers are used to facilitate the identification of each curve. (d) Heat map of $\log(\mathcal{E}(\theta, \omega))$ in the case $p_y = 3$ and $Ro = 1.3 \times 10^{-2}$. The same lines as in figures 1 (b and d) are reported, and a vertical line materialises the angle of the modes closing the triad, that is $-\mathbf{k} \pm \mathbf{p}$.

low imposed wave amplitude (figure 1 a-b), three-dimensional perturbations dominate the growth of the instability. The energy map displays two spots aligned on the dispersion relation with negative frequencies $\omega_{1,2}$ such that $\omega_k + \omega_1 + \omega_2 = 0$ which is indicative of several waves undergoing triadic resonance with the imposed mode. The growth of two-dimensional modes is delayed and their growth rate is approximately twice larger than the rate of three-dimensional modes. Removing the non-linear term $\mathbf{u} \cdot \nabla \mathbf{u}$ (see equation (2.5)) suppresses the growth of two-dimensional modes which are thus not unstable themselves, at least on the timescale of the growth of waves. In fact, we find that $\mathcal{E}_{2d} \simeq 3 \times 10^{-2} (k\mathcal{E}_{3d})^2$ (see figure 1a) in the growth phase which suggests that two-dimensional modes' growth is due to direct forcing by non-linear interaction of two growing waves involved in triadic resonances, with close frequencies and opposed vertical wavenumbers. This mechanism corresponds to the direct excitation of geostrophic modes by two waves identified by Newell (1969) and Smith & Waleffe (1999).

At larger wave amplitude (figure 1c-d), this picture changes: two- and three-dimensional modes grow at the same rate from the start of the simulation. The vertical vorticity field of the growing perturbation and its vertical average are displayed in figure 2a-b. The frequency of two-dimensional modes ($\theta = \pi/2$) is close to 0 according to figure 1d, they are thus geostrophic, that is, slow as well as invariant along the z axis. The geostrophic unstable flow contains the wavevector $\mathbf{p}_g = 2\pi[0, 5, 0]$ (and $-\mathbf{p}_g$ for hermiticity), which grows along with other three-dimensional structures whose energy location in the (θ, ω) space is reminiscent of triadic resonant instability, but with significantly more spreading. Note that the properties of the transition and the instability we report are robust to changes in the aspect ratio of the box, which discards any spurious effect of the discretisation (Smith & Lee 2005).

To further characterise the growth of geostrophic modes, we carry out simulations with the same imposed wave, but we use as initial condition only one wavevector, $\mathbf{p} = 2\pi[0, p_y, 0]$ with $p_y \in \{1, 3, 5\}$ and $s_p = \pm 1$, instead of random noise. The Ekman number is set to 10^{-8} to discard effects of viscosity in the mode growth. The growth rate of geostrophic modes is reported in figure 2c where Ro is systematically varied. At large wave amplitude, the growth rate increases linearly, but it goes to zero at a finite value of $Ro \sim 10^{-2}$. This value is very large compared to the viscous damping $k^2 E \sim 10^{-5}$ which plays no role here, hence suggesting an inviscid mechanism.

On the kinetic energy map $\mathcal{E}(\theta, \omega)$ (figure 2d) two particular spots appear, one at

the location of geostrophic modes and the other at the angle of the vectors closing the triads between \mathbf{k} and $\pm\mathbf{p}_g$, which is indicative of triad-type interactions. This may seem *a priori* in contradiction with the result of Greenspan (1969). Yet, our results are outside Greenspan's theorem framework in two aspects. First, our study is necessarily limited to finite Rossby number. Second, the frequency of the closing mode $-\mathbf{k} \pm \mathbf{p}$ (figure 2d) is outside its eigen frequency. In fact, the discrepancy between the observed and eigen frequencies of the closing mode corresponds to the sum of the eigen frequencies of the three modes, $\Delta\omega_{kpq}$. Moreover, as Ro is decreased, the fastest growing mode \mathbf{p}_g in figure 2c goes from $p_y = 5$ with $\Delta\omega_{kpq} = 0.22$ to $p_y = 1$ with $\Delta\omega_{kpq} = 0.01$: the triad is nearly resonant and draws closer to exact resonance. Two mechanisms may be considered to explain the growth of geostrophic modes. One hypothesis is that the growth of the geostrophic modes is a by-product of a classical resonance between, say, \mathbf{k} and $-\mathbf{q}$ that forces \mathbf{q} (by Hermitian symmetry) and hence \mathbf{p} . However, in this case, the mode closing the wave triad would have an eigen frequency $-\omega_k + \omega_q = \Delta\omega_{kqp} - 2\omega_k$ which is outside the range of inertial waves for small $\Delta\omega_{kpq}$ since $\omega_k \simeq 1.78$. Instead, our results point towards a near-resonant triadic instability that transfers energy from an inertial wave to a z -invariant geostrophic mode.

3. Near-resonance of geostrophic modes: theoretical approach

3.1. The low Rossby number limit

To provide theoretical insight into the inertial-wave destabilisation observed in the numerical simulations, we turn to linear stability analysis. The flow is $\mathbf{U} = \mathbf{u} + Ro\mathbf{U}_w$ where $Ro\mathbf{U}_w$ is the base flow (Ro being the finite Rossby number) and $\mathbf{u} \ll Ro\mathbf{U}_w$ is now an infinitesimal perturbation. We consider a Cartesian domain with periodic boundary conditions and we decompose \mathbf{U} into a superposition of plane waves $\mathbf{h}_p^{s_p} \exp i(\mathbf{p} \cdot \mathbf{x} - \omega_p^{s_p} t)$ with time-dependent amplitudes $b_p^{s_p}(t)$. The Euler equation governing \mathbf{U} is then equivalent to a set of ordinary differential equations governing the amplitudes $b_p^{s_p}$ (Smith & Waleffe 1999):

$$\frac{db_p^{s_p}}{dt} = \sum_{\mathbf{k}+\mathbf{p}+\mathbf{q}=\mathbf{0}} \sum_{s_k, s_q=\pm 1} C_{pkq}^{s_p s_k s_q} b_k^{s_k*} b_q^{s_q*} \exp(i\Delta\omega_{kpq}t) \quad (3.1)$$

$$\text{with } C_{pkq}^{s_p s_k s_q} \equiv \frac{1}{2}(s_q q - s_k k) \mathbf{h}_p^{s_p*} \cdot (\mathbf{h}_k^{s_k*} \times \mathbf{h}_q^{s_q*}) \quad \text{and} \quad \Delta\omega_{kpq} \equiv \omega_k^{s_k} + \omega_q^{s_q} + \omega_p^{s_p}, \quad (3.2)$$

and where $k, p = |\mathbf{k}|, |\mathbf{p}|$. $\Delta\omega_{kpq}$ is the sum of the eigen frequencies of the three modes involved in the triad. In general, maximum energy transfer between the three modes is ensured when the oscillations due to the detuning in the right hand side of (3.1) are cancelled, that is, when $\Delta\omega_{kpq} \rightarrow 0$. If all three modes \mathbf{k} , \mathbf{p} and \mathbf{q} are inertial waves, this leads to the well known mechanism of triadic resonance (Bretherton 1964; Vanneste 2005; Bordes *et al.* 2012). When the mode \mathbf{k} is imposed with an amplitude Ro and helicity s_k , \mathbf{p} and \mathbf{q} grow exponentially with a rate proportional to kRo . This picture is changed when one of the modes, say \mathbf{p} , is geostrophic (*i.e.* $\omega_p^{s_p} = 0$ and $p_z = 0$, regardless of s_p). The spatial interaction condition $\mathbf{k} + \mathbf{p} + \mathbf{q} = \mathbf{0}$ forces $k_z = -q_z$ and the resonance condition becomes

$$\Delta\omega_{kpq} = k_z \left(\frac{s_k}{k} - \frac{s_q}{q} \right) = \omega_k \frac{1}{q} \left(q - \frac{s_q}{s_k} k \right) \rightarrow 0. \quad (3.3)$$

It may be fulfilled only when $s_q = s_k$ and $q - k \rightarrow 0$. At exact resonance, these conditions impose \mathbf{p} to be located on a circle centred on $-\mathbf{k}_\perp = -[k_x, k_y]$ with radius $|\mathbf{k}_\perp|$.

Moreover, in the governing equation for $\dot{b}_p^{s_p}$, the slow oscillation terms involve a coupling coefficient $C_{pkq}^{s_p s_k s_k} \propto k - q \rightarrow 0$. At exact resonance, the coupling coefficient vanishes: there is no energy transfer from waves to geostrophic modes, as proved by Greenspan (1969).

Nevertheless, wave-to-geostrophic transfer is still possible when the detuning $\Delta\omega_{kpq}$ is small but non-zero (Newell 1969; Smith & Waleffe 1999; Alexakis 2015), and we investigate instabilities of geostrophic modes driven by this mechanism. Let us assume that the wave \mathbf{k} with helicity s_k is imposed with a small constant amplitude Ro , and that \mathbf{p} is geostrophic. To infer from (3.1) the time evolution of the geostrophic mode amplitude, we proceed to an asymptotic expansion using a two-time method involving a fast time $\tau = t$ and a slow time T . The hierarchy between them must be a power of kRo , the intrinsic Rossby number based on the imposed wavelength. Because the wave-to-geostrophic transfer coefficient $C_{pkq}^{s_p s_k s_k}$ vanishes as $\Delta\omega_{kpq} \rightarrow 0$, we find via a heuristic analysis detailed in appendix A that $T = (kRo)^2 t$, instead of $(kRo)t$ for classical wave triads. In addition, it imposes the amplitude of \mathbf{p} to be smaller by a factor kRo compared to the mode closing the triad $\mathbf{q} = -\mathbf{k} - \mathbf{p}$. The amplitudes of the modes interacting with the imposed waves (\mathbf{p} and \mathbf{q} with both helicity signs $s_{p,q}$) are thus expanded as

$$\begin{cases} b_q^{s_q} &= (kRo)B_{q1}^{s_q}(T, \tau) + (kRo)^3 B_{q2}^{s_q}(T, \tau) \\ b_p^{s_p} &= (kRo)^2 B_{p1}^{s_p}(T, \tau) + (kRo)^4 B_{p2}^{s_p}(T, \tau) \end{cases} \quad (3.4)$$

where the B_i^j are all $O(1)$. The hierarchy between orders is imposed by the need to match the slow time derivative of the leading order with the next order in the multiple scale expansion. Since the slow derivation introduces a factor $(kRo)^2$, there must be a $(kRo)^2$ hierarchy between the first and second orders.

To find the equations governing the leading order coefficients, we follow the method of Bretherton (1964) and inject the ansatz (3.4) into (3.1). First, the leading order coefficients are found to be independent of τ and their long time evolution with T is determined at next order. As noted by Bretherton (1964), for fast triads with detuning larger than $O((kRo)^2)$, the imposed wave only drives fast and bounded oscillations of the second order terms, and the leading order terms must be zero to avoid secular growth. It is only for slow triads, *i.e.* when $\Delta\omega_{kpq} = O((kRo)^2)$, that the exponential term in equation (3.1) drives slow oscillations that contribute to secular growth. Such a condition on the detuning is consistent with the numerics: the fastest growing modes at $Ro = 1 \times 10^{-2}$ ($kRo \sim 0.6$) in figure 2c is $\mathbf{p} = 2\pi[0, 3, 0]$ for which $\Delta\omega_{kpq} \simeq 0.1 \sim 0.3(kRo)^2$. The condition $\Delta\omega_{kpq} = O((kRo)^2)$ may be fulfilled only for the modes \mathbf{p} with $s_p = \pm 1$ and \mathbf{q} with $s_q = s_k$ and, as noted earlier, the wave-to-geostrophic transfer coefficient $C_{pkq}^{s_p s_k s_k}$ is also $O((kRo)^2)$. Cancelling the secular growth terms at second order gives the following amplitude equations,

$$\partial_T B_{q1}^{s_q} = \sum_{s_p} C_{qkp}^{s_k s_k s_p} B_{p1}^{s_p} * e^{i \frac{\Delta\omega_{kpq}}{(kRo)^2} T} \quad \text{and} \quad \partial_T B_{p1}^{s_p} = \frac{C_{pkq}^{s_p s_k s_k}}{(kRo)^2} B_{q1}^{s_q} * e^{i \frac{\Delta\omega_{kpq}}{(kRo)^2} T}, \quad (3.5)$$

the rescaled quantities $C_{pkq}^{s_p s_k s_k} / (kRo)^2$ and $\Delta\omega_{kpq} / (kRo)^2$ being $O(1)$. These equations have exponentially growing solutions and the complex growth rate of the instability normalised by the rotation rate is

$$\sigma = i \frac{\Delta\omega_{kpq}}{2} + \frac{1}{2} \sqrt{4 \sum_{s_p} C_{pkq}^{s_p s_k s_k} C_{qkp}^{s_k s_k s_p} * Ro^2 - \Delta\omega_{kpq}^2} \equiv i \frac{\Delta\omega_{kpq}}{2} + \sigma_k(\mathbf{p}; Ro). \quad (3.6)$$

Note that the product of coupling coefficients $C_{pkq}^{s_p s_k s_k} C_{qkp}^{s_k s_k s_p} *$ is real. The expression of the real part of growth rate, $\sigma_k(\mathbf{p}; Ro)$, is consistent with the numerical findings: for a

given near-resonant triad, it drops to zero at a finite value of Ro and it is proportional to Ro at large Ro . However, in the small Rossby number limit, because the detuning $\Delta\omega_{kpq}$ and the coupling coefficient $C_{pkq}^{s_p s_k s_k}$ are both $O((kRo)^2)$, the maximum geostrophic growth rate remains $O((kRo)^2)$ at most.

The $(kRo)^2$ scaling governing the maximum growth rate of geostrophic near-resonance is found quantitatively by expanding the frequency detuning, the transfer coefficients and then $\sigma_k(\mathbf{p}; Ro)$ in the neighbourhood of exact resonance. The fact that the growth rate is non-zero only close to the exact resonance is illustrated qualitatively in figure 3a. We thus introduce $\mathbf{p} = \mathbf{p}_0 + (kRo)^2 \delta\mathbf{p}$ where $\delta\mathbf{p}$ is a $O(1)$ vector in the geostrophic plane. Consider the closing modes $\mathbf{q}_0 = -(\mathbf{k} + \mathbf{p}_0)$ and $\mathbf{q} = -(\mathbf{k} + \mathbf{p})$, then $\mathbf{q} = \mathbf{q}_0 - (kRo)^2 \delta\mathbf{p}$. The imposed mode \mathbf{k} is left unperturbed. Since $\Delta\omega_{kpq} = C_{p_0 k q_0}^{s_p s_k s_k} = 0$ at exact resonance, the leading orders of the frequency detuning and the transfer coefficients are found from (3.2) and (3.3) to be $O((kRo)^2)$. The perturbation of the wavevectors is thus consistent with the asymptotic expansion. At leading order,

$$\frac{\Delta\omega_{kpq}}{(kRo)^2} \simeq s_k \omega_k \frac{\mathbf{q}_0 \cdot \delta\mathbf{p}}{k^2} \quad \text{and} \quad \frac{C_{pkq}^{s_p s_k s_k}}{(kRo)^2} \simeq \frac{1}{2} s_k (\mathbf{h}_{p_0}^{s_p} \cdot (\mathbf{h}_k^{s_k} \times \mathbf{h}_{q_0}^{s_k})) \frac{\mathbf{q}_0 \cdot \delta\mathbf{p}}{k}, \quad (3.7)$$

where we have used that $q_0 = k$ and $s_q = s_k$. In the growth rate $\sigma_k(\mathbf{p}; Ro)$, the product of the coupling coefficient is

$$\sum_{s_p} C_{pkq}^{s_p s_k s_k} C_{qkp}^{s_k s_k s_p} \simeq \frac{1}{4} (kRo)^2 k^2 \frac{\mathbf{q}_0 \cdot \delta\hat{\mathbf{p}}}{k^2} \sum_{s_p} \left(1 - s_p \frac{p_0}{k}\right) |\mathbf{h}_{p_0}^{s_p} \cdot (\mathbf{h}_k^{s_k} \times \mathbf{h}_{q_0}^{s_k})|^2. \quad (3.8)$$

Therefore, at leading order in powers of Ro , the growth rate is

$$4\sigma_k(\mathbf{p}; Ro)^2 = (\mathcal{C}_k(\mathbf{p}_0)X - \omega_k^2 X^2)(kRo)^4, \quad (3.9)$$

where $X \equiv (\mathbf{q}_0 \cdot \delta\mathbf{p})/k^2$ and $\mathcal{C}_k(\mathbf{p}_0)$ is the sum in the right hand side of (3.8). When $\mathcal{C}_k(\mathbf{p}_0) > 0$, the growth rate reaches an optimum at $X = \mathcal{C}_k/(2\omega_k^2)$ with value $(kRo)^2 \mathcal{C}_k(\mathbf{p}_0)/|4\omega_k|$, which remains to be maximised over all exactly resonant wavevectors \mathbf{p}_0 . The coefficient $\mathcal{C}_k(\mathbf{p}_0)$ is shown in figure 3b for several wavevectors \mathbf{k} with different frequencies ω_k . When plotted against p_0/k_\perp , all the curves \mathcal{C}_k collapse on a master curve that reaches a maximum value of 1 at $p_0 \rightarrow 0$, regardless of the helicity sign s_k of the imposed wave. As $(kRo) \rightarrow 0$, the unstable geostrophic mode becomes large-scale and stems from the interaction between \mathbf{k} and $\mathbf{q} \simeq -\mathbf{k}$. In the low Rossby number limit, the maximal growth rate is then

$$\sigma_k^{\max}(Ro) = \frac{1}{4} \frac{(kRo)^2}{|\omega_k|}. \quad (3.10)$$

We confirm that kRo , the Rossby number based on the wavelength, is the relevant parameter to describe the growth rate of the instability. While each geostrophic mode follows the law (3.6), all the growth rate curves lie below a $(kRo)^2$ upper envelope. More details are given below in section 3.3 where we compare the law (3.10) to exact computation of the growth rate curves from (3.6).

3.2. The moderate to large Rossby number regime

The Ro^2 law governing the growth rate in the small Rossby number limit cannot hold as the wave amplitude is increased since the growth rate has an upper bound following a Ro law. This is proven directly by multiplying (2.5) by \mathbf{u} and integrating over the fluid

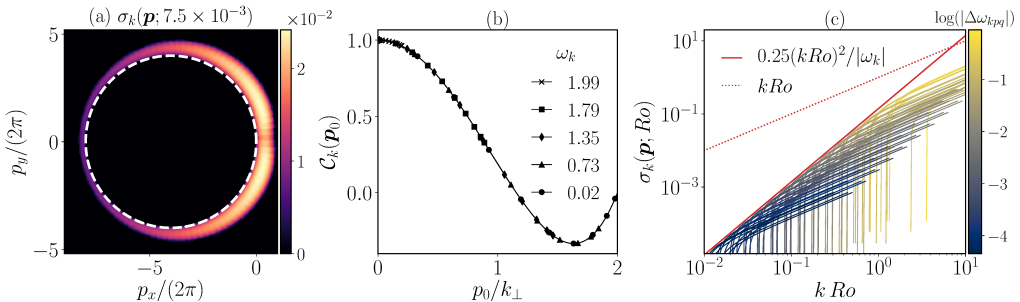


FIGURE 3. (a) Map of the growth rate of geostrophic modes at $Ro = 7.5 \times 10^{-3}$ computed from (3.6). The imposed wave is $2\pi [4, 0, 8]$. The white dashed circle locates the exactly resonant geostrophic modes. The color scale gives the amplitude of the growth rate. Where it is maximum ($p_x = 0, p_y \simeq \pm 2$), the detuning is about $0.04 \sim 0.24(kRo)^2$. (b) Plot of $C_k(\mathbf{p}_0)$ on the exact resonant circle against p_0 normalised by the horizontal wavenumber k_\perp for several wavevectors \mathbf{k} with different frequencies ω_k . The curve is the same regardless of the imposed helicity sign s . (c) Growth rate curves of the geostrophic modes as a function of the Rossby number. The geostrophic modes are sampled over 15 circles whose centers are the same as the exact resonance circle with 5 points on each circle. The line colour codes the frequency detuning $|\Delta\omega_k|$. The upper envelope is compared to the law (3.10) and the upper bound (3.12).

domain V , thus giving:

$$\sigma = \frac{1}{2} \frac{d \ln \|\mathbf{u}\|_2^2}{dt} = -\frac{Ro}{\|\mathbf{u}\|_2^2} \int_V \mathbf{u} \cdot \nabla \mathbf{U}_w \cdot \mathbf{u} \quad (3.11)$$

where $\|\cdot\|_n$ denotes the L_n -norm. In virtue of Hölder's inequality (Gallet 2015),

$$|\sigma| \leq Ro \|\nabla \mathbf{U}_w\|_\infty \leq kRo \quad (3.12)$$

This upper bound applies in particular to the low Ro scaling (3.10), which thus holds up to $kRo \sim 1$ at most. Note that, beyond that point, non-triad type instabilities (shear, centrifugal) may add to near-resonance in driving the dynamics of the flow excited by the maintained wave.

3.3. Comparison with exact computation

In figure 3, we sample the growth rate curves given by (3.6) of many geostrophic modes in near resonant interaction with $\mathbf{k} = 2\pi [4, 0, 8]$, as functions of the Rossby number. We notice that each growth rate curve follows a Ro scaling at sufficiently large Ro , which is consistent with the asymptotic expansion carried out in section 3.1. However, because for all modes the growth rate vanishes at a finite value of Ro (which decreases to 0 close to exact resonance), the upper envelope is a Ro^2 law that perfectly matches the theoretical prediction (3.10). This instability is thus fundamentally different from four-modes interactions for which each growth rate curve follows a Ro^2 law (Kerswell 1999; Brunet *et al.* 2020). Besides, in agreement with the upper bound (3.12), we observe the Ro^2 maximum growth rate law to break down above $kRo \sim 1$. Beyond that, the near-resonance growth rate derived from (3.6) remains below the upper bound and follows a Ro law. However, additional instabilities (shear, centrifugal, etc.) may also drive the growth of geostrophic modes in this regime.

3.4. Finite size and viscous effects

Finite size domain translates into discretisation of the modes. Since the exactly resonant geostrophic modes lie on a finite radius circle, they cannot be approached with

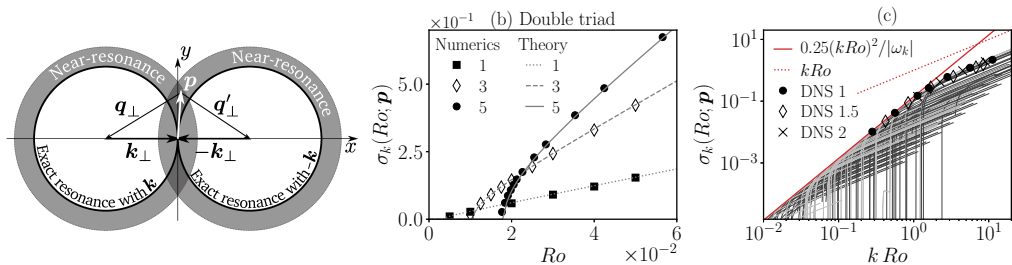


FIGURE 4. (a) Schematic cartoon of a geostrophic mode \mathbf{p} in near-resonance with both imposed modes $\pm\mathbf{k}$ at the same time, based on the map of figure 3a. The \perp indices denote the horizontal component of wavevectors. (b) Comparison between theory (4.4) and the direct numerical simulations of figure 2c. The imposed wave is $\mathbf{k} = 2\pi [4, 0, 8]$ and the geostrophic modes are $\mathbf{p} = 2\pi [0, p_y, 0]$, p_y being given in the legend. (c) Samples of the growth rate curves $\sigma_k(\mathbf{p}; Ro)$ of modes \mathbf{p} interacting with $\pm\mathbf{k} = 2\pi [4, 0, 8]$ including simple (dark grey) and double (light grey) triad mechanisms. The double triad growth rate curves are determined by finding the roots of \mathcal{P} (see equation (4.2)) for wavevectors \mathbf{p} restricted to $|p_x| < \pi$ and $|p_y| < 12\pi$. We recall the Ro^2 law (3.10) and the growth rate upper bound (3.12). The dots represent the geostrophic growth rate found in the DNS with imposed wave vector $\mathbf{k} = 2\pi [4, 0, 8]$ (DNS 1), $\mathbf{k} = 1.5 \times 2\pi [4, 0, 8]$ (DNS 1.5) and $\mathbf{k} = 2 \times 2\pi [4, 0, 8]$ (DNS 2).

arbitrarily low detuning $\Delta\omega_{kpq}$ as $Ro \rightarrow 0$. Hence, discretisation implies the existence of a finite value of Ro below which the near-resonant instability vanishes. Regarding viscous effects, at finite but low Ekman number, *i.e.* when $(kRo)^2 \gg k^2E$, the low Rossby number scaling is unaltered since the near-resonant modes \mathbf{p} and \mathbf{q} have at most similar wavenumbers to \mathbf{k} . The $O(Ro)$ upper bound on the growth rate is also unaltered by the inclusion of viscosity.

4. A refined model: the double near-resonant triad

Although promising, the model of the previous section needs to be refined to fully account for numerical results. It misses by a factor two the growth rate curves of figure 2c and (3.6) predicts a frequency $\Delta\omega_{kpq}/2 \neq 0$ for the geostrophic modes, while it is 0 according to figure 2d. We must include in our model that not only \mathbf{k} , but also $-\mathbf{k}$ (with the same helicity sign s) is imposed due to Hermitian symmetry. Consider two triads $\mathbf{k} + \mathbf{p} + \mathbf{q} = \mathbf{0}$ and $-\mathbf{k} + \mathbf{p} + \mathbf{q}' = \mathbf{0}$ (see figure 4) with helicity signs $s_q = s_{q'} = s$ and $s_p = \pm 1$. As shown schematically in figure 4a, the exact resonance circles associated to $\pm\mathbf{k}$ coincide at $\mathbf{p} = \mathbf{0}$. In a neighbourhood of this point (the dark grey intersection in figure 4a), a geostrophic mode \mathbf{p} is in near-resonance with both $\pm\mathbf{k}$ with both detunings $\Delta\omega_{kpq}$ and $\Delta\omega_{-kpq'}$ small. This is all the more important that $\mathbf{p} = \mathbf{0}$ corresponds to the largest near-resonant growth rate as $Ro \rightarrow 0$.

In a very similar way to the two-time asymptotic expansion of section 3.1, we can retrieve the amplitude equations governing the slowly varying envelopes $B_{p1}^{s_p}$ and $B_{Q1}^{s_Q}$, with $\mathbf{K} = \pm\mathbf{k}$, $\mathbf{Q} = -\mathbf{K} - \mathbf{p}$, and $s_p = \pm 1$. Similarly to (3.5), the four amplitude equations are

$$\begin{cases} \partial_T B_{Q1}^{s_K} &= \sum_{s_p=\pm 1} C_{QKp}^{s_K s_K s_p} B_{p1}^{s_p *} e^{i \frac{\Delta\omega_{KpQ}}{(kRo)^2} T}, \\ \partial_T B_{p1}^{s_p} &= \sum_{\mathbf{K}=\pm\mathbf{k}} \frac{C_{pKQ}^{s_p s_K s_K}}{(kRo)^2} B_{Q1}^{s_K *} e^{i \frac{\Delta\omega_{KpQ}}{(kRo)^2} T}. \end{cases} \quad (4.1)$$

The characteristic polynomial $\mathcal{P}(\sigma)$ of this set of four linear differential equations in

terms of the Rossby number Ro and the detunings $\Delta\omega_K$ is:

$$\mathcal{P}(\sigma) = (\sigma^2 - i\Delta\omega_{kpq}\sigma - Ro^2 S_k) (\sigma^2 - i\Delta\omega_{-kpq'}\sigma - Ro^2 S_{-k}) - Ro^4 P_0, \quad (4.2)$$

with S_K and P_0 two real coefficients defined as

$$S_K = \sum_{s_p} C_{pKQ}^{s_p s_k s_k} C_{QKp}^{s_k s_k s_p *} \quad \text{and} \quad P_0 = \left(\sum_{s_p} C_{qkp}^{s_k s_k s_p} C_{p-kq'}^{s_p s_k s_k} \right) \left(\sum_{s_p} C_{q'-kp}^{s_k s_k s_p} C_{pkq}^{s_p s_k s_k} \right). \quad (4.3)$$

In general, the growth rate $\sigma_k(\mathbf{p}; Ro)$ is found by numerical computation of the roots of \mathcal{P} . Nevertheless, an estimate of the maximum growth rate can be obtained in the limit $|p_x| \ll |p_y|$, which is relevant to our DNS. In this case, symmetries impose $\Delta\omega_{kpq} = -\Delta\omega_{-kpq'}$, $S_k = S_{-k}$ and $P_0 = S_k^2$. The polynomial \mathcal{P} then has a purely real root,

$$\sigma_k(\mathbf{p}; Ro) = \sqrt{2Ro^2 S_k(\mathbf{p}) - \Delta\omega_{kpq}^2} \quad (4.4)$$

and the frequency of the growing geostrophic mode is then 0. We show in figure 4b the excellent agreement between this theoretical law and the DNS data of figure 2a. An expansion similar to section 3.1 reveals that the maximum growth rate follows the exact same $(kRo)^2$ law as in the case of the single triad (3.10). This is confirmed by the systematic computation of the growth rate in the double triad case, as shown in figure 4c. Note that although this instability is driven by two imposed modes, it remains different from the four-modes interaction mechanism detailed in Brunet *et al.* (2020). The latter features intermediate, non-resonant modes that are absent in the double triad mechanism. Moreover, the near-resonant growth rate (4.4) is proportional to Ro when Ro is sufficiently large, whereas it always follows a Ro^2 law in the case of four-modes interaction.

We compare in figure 4c our theoretical predictions with the geostrophic growth rate extracted from DNS initiated with a large-scale noise, as in section 2, down to $Ro = 5 \times 10^{-3}$. We use the same imposed wave vector as previously ($\mathbf{k} = 2\pi[4, 0, 8]$) but also 1.5 and 2 times longer wavevectors to confirm that the growth rate is a function of the intrinsic Rossby number kRo . Such a dependence is expected since in the infinite-domain limit, $L \rightarrow \infty$, L becomes irrelevant and $1/k$ is the only remaining length scale, and the associated Rossby number is kRo . As shown in figure 4c, the numerical growth rate coincides with the maximum near-resonant growth rate in the low Ro regime but also in the moderate Ro regime where it is proportional to kRo . Note that for the three lowest kRo points, the noise has been implemented on two-dimensional modes ($p_z = 0$) to facilitate the isolation of the geostrophic instability. It delays the growth of two-dimensional modes with non-zero frequency by direct forcing at the lowest values of Ro . Despite their rapid growth, the latter are subdominant in the saturation of wave-driven flows, and do not prevent the long-term growth of unstable geostrophic modes under the mechanism examined here.

Lastly, our analysis allows us to understand the transition in the stability of the geostrophic flow observed in the numerical study (see figure 1). $Ro = 2.83 \times 10^{-2}$ ($kRo \simeq 1.6$) corresponds to the transition zone where the geostrophic growth rate is $O(kRo)$, as the wave-only triadic resonances (see figure 4c). When the Rossby number is decreased by one order of magnitude, as shown in figure 4c, the growth rate of geostrophic modes scales like $(kRo)^2$, *i.e.* a factor kRo smaller than the growth rate of wave-only triadic resonances. This is why the geostrophic instability is not observed in the simulation at $Ro = 2.83 \times 10^{-3}$.

5. Conclusion

By means of numerical simulations and theoretical analysis, we have described a new instability mechanism by which inertial waves excite z -invariant geostrophic modes. We have proved that this instability is driven by near-resonant triadic interaction and derived its theoretical growth rate. When normalised by the global rotation rate Ω , the growth rate follows a $(kRo)^2$ law and a kRo law at small and moderate wave amplitude, respectively, k being the imposed wavenumber. It translates into Ω^{-1} and Ω^0 laws, respectively, for the dimensional growth rate. The near-resonant instability completes the picture proposed in Brunet *et al.* (2020) where another inviscid geostrophic instability based on two imposed modes and four-modes interaction is detailed. Although of different nature, both instabilities have a $(kRo)^2$ growth rate in the limit of small Rossby numbers which makes them possibly difficult to distinguish. On the one hand, in the linear growth phase, the eigenmode of the four-mode instability consists of waves and geostrophic flow of comparable amplitude, whereas the geostrophic flow is kRo times smaller than the waves in the present mechanism. On the other hand, the near-resonant instability achieves a growth rate of order kRo for $kRo \gtrsim 1$. Our analysis may thus explain the experimental results of Le Reun *et al.* (2019): they found at moderate Rossby number a geostrophic instability with a growth rate proportional to Ro , which thus matches the moderate Rossby number law derived here.

Our work paves the way for new studies dealing with the energy transfers from waves to geostrophic modes in rotating fluids, in particular in rotating turbulence. First, it remains to be seen under which conditions the near-resonant instability may excite slow nearly geostrophic modes with small but non-zero frequencies. These modes have been proved to be important for the development of anisotropy in rotating turbulence (Smith & Lee 2005) even in the asymptotic limit of small Rossby numbers (van Kan & Alexakis 2019).

With a heuristic analysis similar to the one developed in section 3.1 and appendix A, we can predict again a $(kRo)^2$ growth rate, but a detailed analysis is difficult and remains to be done. Lastly, the instability we describe in the present article could play an important role in the rotating turbulence dynamics that remains to be fully deciphered. Since wave-wave triadic interactions grow at rate $O(kRo)$ while wave-geostrophic interactions have a $O((kRo)^2)$ growth rate, we may speculate that, at sufficiently low forcing amplitudes, rotating turbulence may remain purely three-dimensional as the wave amplitudes would remain below the threshold of geostrophic instabilities. Such states have been observed by Le Reun *et al.* (2017, 2019) and Brunet *et al.* (2020), but a systematic investigation of their existence in various realisations of rotating turbulence remains to be carried out. In the future, our study could help bridging the gap between finite Rossby number experiments and simulations of turbulence (Godeferd & Moisy 2015) and asymptotic models of rotating turbulence (Galtier 2003; Bellet *et al.* 2006; van Kan & Alexakis 2019).

Acknowledgement. The authors acknowledge funding by the European Research Council under the European Union’s Horizon 2020 research and innovation program through Grant No. 681835-FLUDYCO-ERC-2015-CoG and FLAVE 757239. TLR is supported by the Royal Society through a Newton International Fellowship (Grant reference NIF\R1\192181).

Declaration of Interests. The authors report no conflict of interest.

Appendix A. Heuristic justification of the $(kRo)^2$ slow timescale

To investigate near-resonant instability, we proceed to an asymptotic expansion of the

spectral version of the Euler equation using a two-timing methods involving a fast time $\tau = t$ and a slow time T . The hierarchy between τ and T may be derived heuristically from an analysis of the amplitude equation in a triad involving a geostrophic mode. Let us assume the amplitudes $b_{p,q}$ to scale like $\varepsilon_{p,q}$ and that the slow time is given by the small detuning, $\Delta\omega_{kpq} = O(\beta)$. We further assume that $\beta, \varepsilon_{p,q} = O(kRo)$ at least. The two amplitude equations stemming from (3.1) governing $b_{p,q}$ give the following scaling relationships:

$$\beta\varepsilon_p = kRo\beta\varepsilon_q \quad \text{and} \quad \beta\varepsilon_q = kRo\varepsilon_p \quad (\text{A } 1)$$

where we have used that the wave-to-geostrophic coupling coefficient is proportional to the detuning, hence β , as explained in section 3.1 below equation (3.3). We have also used that the coupling coefficients scale like the wavenumber k . For the hierarchy between $\varepsilon_{p,q}$ and β to hold, the determinant of the system (A 1) with unknowns $\varepsilon_{p,q}$ must vanish. This condition is satisfied when $\beta = (kRo)^2$. When this condition is satisfied, the equation (A 1) yields $\varepsilon_p = kRo\varepsilon_q$. Therefore, we chose the amplitudes b_p^{sp} and b_q^{sq} to scale like $(kRo)^2$ and kRo respectively at leading order.

REFERENCES

- ALEXAKIS, A. 2015 Rotating Taylor–Green flow. *Journal of Fluid Mechanics* **769**, 46–78.
- BELLET, F., GODEFERD, F. S., SCOTT, J. F. & CAMBON, C. 2006 Wave turbulence in rapidly rotating flows. *Journal of Fluid Mechanics* **562**, 83–121.
- BORDES, G., MOISY, F., DAUXOIS, T. & CORTET, P.-P. 2012 Experimental evidence of a triadic resonance of plane inertial waves in a rotating fluid. *Physics of Fluids* **24** (1), 014105.
- BRETHERTON, F. P. 1964 Resonant interactions between waves. The case of discrete oscillations. *Journal of Fluid Mechanics* **20** (3), 457–479.
- BRUNET, M., GALLET, B. & CORTET, P.-P. 2020 Shortcut to Geostrophy in Wave-Driven Rotating Turbulence: The Quartetic Instability. *Physical Review Letters* **124** (12), 124501.
- CAMBON, C. & JACQUIN, L. 1989 Spectral approach to non-isotropic turbulence subjected to rotation. *Journal of Fluid Mechanics* **202**, 295–317.
- CLARK DI LEONI, P. & MININNI, P. D. 2016 Quantifying resonant and near-resonant interactions in rotating turbulence. *Journal of Fluid Mechanics* **809**, 821–842.
- FAVIER, B., GUERVILLY, C. & KNOBLOCH, E. 2019 Subcritical turbulent condensate in rapidly rotating Rayleigh–Bénard convection. *Journal of Fluid Mechanics* **864**.
- GALLET, B. 2015 Exact two-dimensionalization of rapidly rotating large-Reynolds-number flows. *Journal of Fluid Mechanics* **783**, 412–447.
- GALTIER, S. 2003 Weak inertial-wave turbulence theory. *Physical Review E* **68** (1).
- GODEFERD, F. S. & MOISY, F. 2015 Structure and Dynamics of Rotating Turbulence: A Review of Recent Experimental and Numerical Results. *Applied Mechanics Reviews* **67** (3), 030802–030802.
- GREENSPAN, H. P. 1969 On the non-linear interaction of inertial modes. *Journal of Fluid Mechanics* **36** (02), 257–264.
- KERSWELL, R. R. 1999 Secondary instabilities in rapidly rotating fluids: Inertial wave breakdown. *Journal of Fluid Mechanics* **382**, 283–306.
- LE REUN, T., FAVIER, B., BARKER, A. J. & LE BARS, M. 2017 Inertial Wave Turbulence Driven by Elliptical Instability. *Physical Review Letters* **119** (3), 034502.
- LE REUN, T., FAVIER, B. & LE BARS, M. 2019 Experimental study of the nonlinear saturation of the elliptical instability: Inertial wave turbulence versus geostrophic turbulence. *Journal of Fluid Mechanics* **879**, 296–326.
- LESUR, G. & LONGARETTI, P.-Y. 2005 On the relevance of subcritical hydrodynamic turbulence to accretion disk transport. *Astronomy and Astrophysics* **444** (1), 25–44.
- NEWELL, A. C. 1969 Rossby wave packet interactions. *Journal of Fluid Mechanics* **35** (2), 255–271.
- SAGAUT, P. & CAMBON, C. 2018 *Homogeneous Turbulence Dynamics*, 2nd edn. Springer International Publishing.

- SMITH, L. M. & LEE, Y. 2005 On near resonances and symmetry breaking in forced rotating flows at moderate Rossby number. *Journal of Fluid Mechanics* **535**, 111–142.
- SMITH, L. M. & WALEFFE, F. 1999 Transfer of energy to two-dimensional large scales in forced, rotating three-dimensional turbulence. *Physics of Fluids* **11** (6), 1608–1622.
- VAN KAN, A. & ALEXAKIS, A. 2019 Critical transition in fast-rotating turbulence within highly elongated domains. *arXiv:1912.05394 [physics]* , arXiv: 1912.05394.
- VANNESTE, J. 2005 Wave Interactions. In *Nonlinear Waves in Fluids: Recent Advances and Modern Applications* (ed. Roger Grimshaw), pp. 69–94. Vienna: Springer Vienna.
- WALEFFE, F. 1992 The nature of triad interactions in homogeneous turbulence. *Physics of Fluids A: Fluid Dynamics* **4** (2), 350–363.
- YAROM, E. & SHARON, E. 2014 Experimental observation of steady inertial wave turbulence in deep rotating flows. *Nature Physics* **10** (7), 510–514.
- YOKOYAMA, N. & TAKAOKA, M. 2017 Hysteretic transitions between quasi-two-dimensional flow and three-dimensional flow in forced rotating turbulence. *Physical Review Fluids* **2** (9), 092602.